

Supplementary Information for:

**A New 3D Dirac Nodal-line Semimetallic Graphene Monolith for Lithium Ion
Battery Anode Material**

Jie Liu¹, Xiaoyin Li¹, Qiang Wang^{1*}, Yoshiyuki Kawazoe², and Puru Jena³

¹Center for Applied Physics and Technology, Department of Materials Science and Engineering, HEDPS, BKL-MEMD, College of Engineering, Peking University; Beijing 100871, China

²New Industry Creation Hatchery Center, Tohoku University, Sendai, 980-8577, Japan

³Department of Physics, Virginia Commonwealth University, Richmond, VA 23284, USA

* Correspondence: qianwang2@pku.edu.cn

SI Text

Text S1 The relationship between the band crossing point and time reversal and space inversion symmetries.

Neglecting the weak spin-orbit coupling, the band crossing point in HAGM-42 is fourfold degenerate, which is protected by the coexistence of time reversal and space inversion symmetries. If the required symmetry constraints are broken, the degeneracy will be destroyed and a band gap may open up. To verify this, we artificially break the time reversal and space inversion symmetries of HAGM-42, and calculate the corresponding electronic band structures. The time reversal symmetry is broken by doping HAGM-42 with Mn atoms as a magnetic impurity (see Fig. S4a). The resulting band structures, plotted in Fig. S4b, show that the spin up and down bands are split and the pristine four-fold degenerate band crossing point is decomposed to two two-fold degenerate points. In contrast, when the dopant is replaced with a nonmagnetic element like Li, the four-fold degenerate point still remains, as shown in Fig. S4c. To break the space inversion symmetry, we make a small movement for some atoms in HAGM-42, as shown in Fig. S5a, and calculate its electronic band structure. The results in Fig. S5b clearly show that a gap is opened up because of the breakage of space inversion

symmetry.

SI Table

Table S1 Lattice parameters (a , b and c , in Å) for HZGM-42, diamond, and graphite calculated using different exchange-correction functionals.

Methods		HZGM-42	Diamond	Graphite
PBE	a	16.82	4.28	2.46
	b	16.82	4.28	2.46
	c	2.47	4.28	8.35
PBE-D2	a	16.79	4.27	2.46
	b	16.79	4.27	2.46
	c	2.46	4.27	6.41

SI Figures

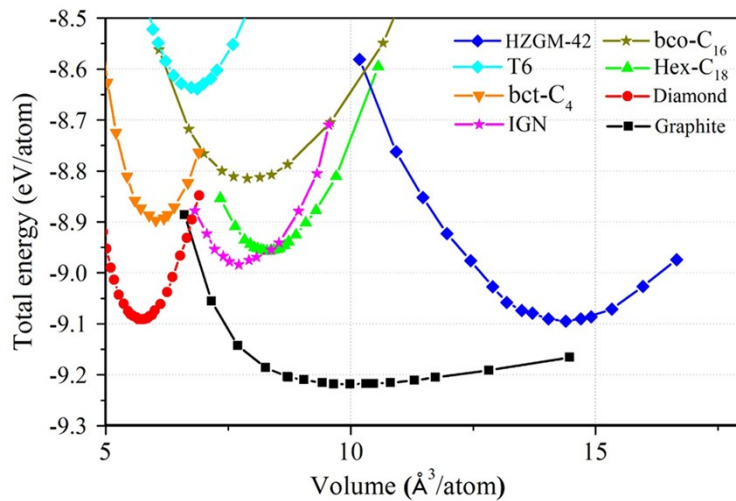


Fig. S1 Calculated total energy versus volume per atom for HZGM-42, graphite, diamond, T6, bct-C₄, IGN, bco-C₁₆, and Hex-C₁₈.

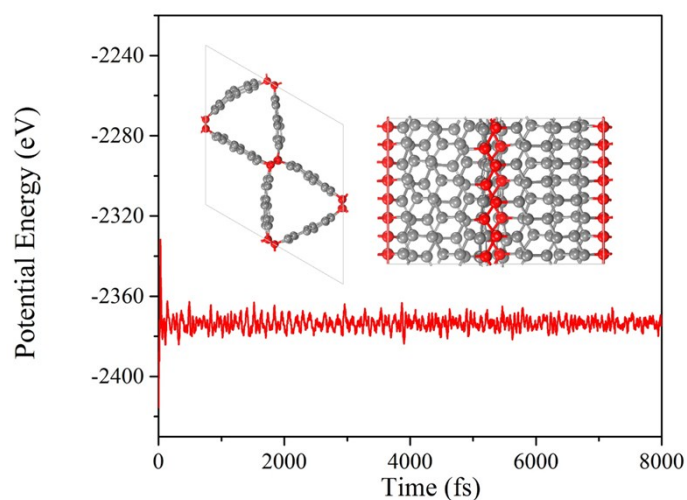


Fig. S2 Total potential energy fluctuation during AIMD simulation at 1200 K of HZGM-42. The inset shows the atomic configurations ($1 \times 1 \times 4$ supercell for HZGM-42) at the end of AIMD simulations at 1200 K.

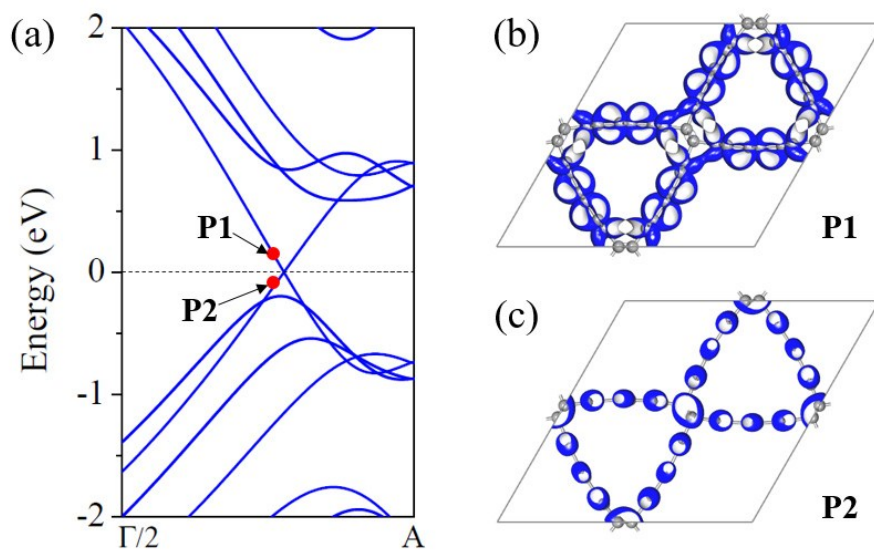


Fig. S3 (a) Band structure of HAGM-42 along the high symmetric path $\Gamma/2 \rightarrow A$. (b) and (c) Charge densities of P1 and P2 states, respectively. The isosurface value is $0.005 \text{ e}/\text{\AA}^3$.

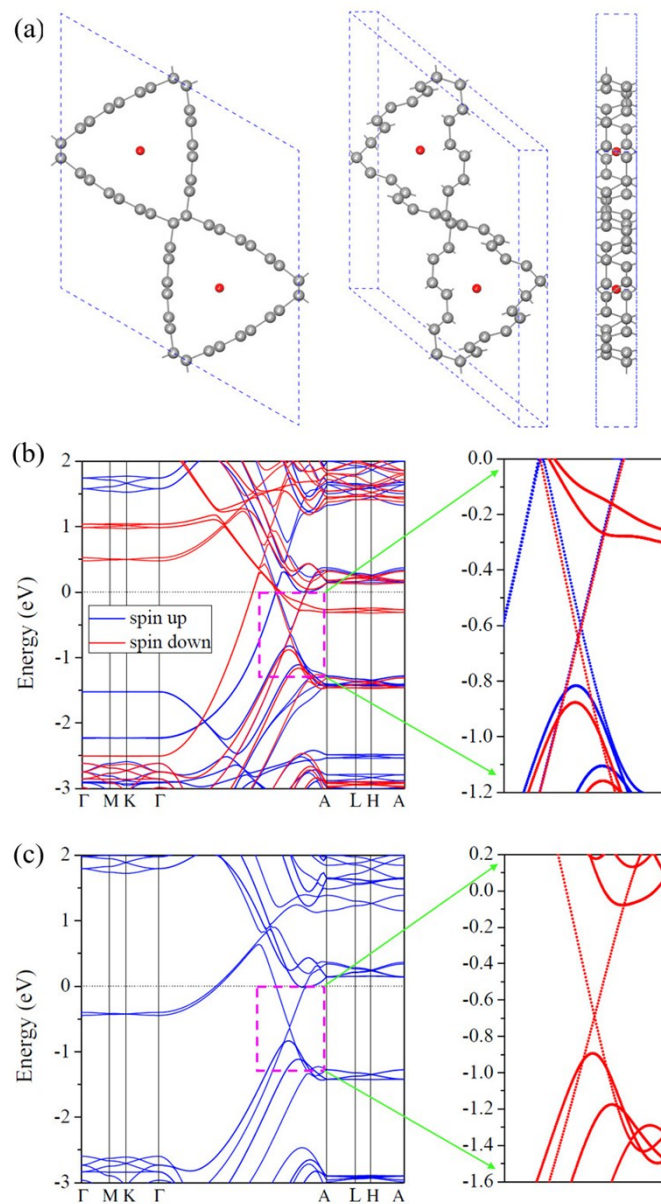


Fig. S4 (a) Structure of Mn-doped HAGM-42. (b) and (c) Electronic band structures of Mn- and Li-doped HAGM-42, respectively.

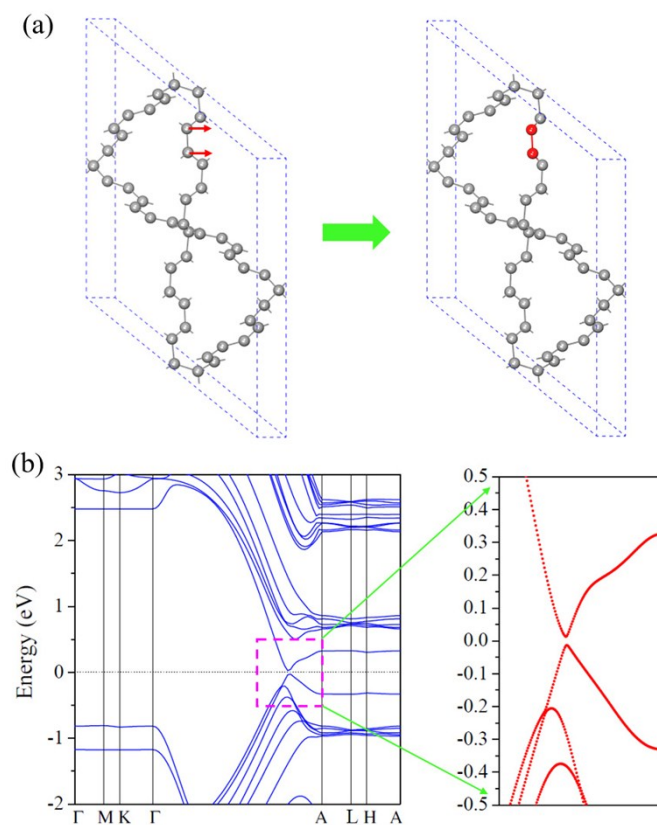


Fig. S5 (a) Illustration of atomic movement in HAGM-42, and (b) the resulting electronic band structure.

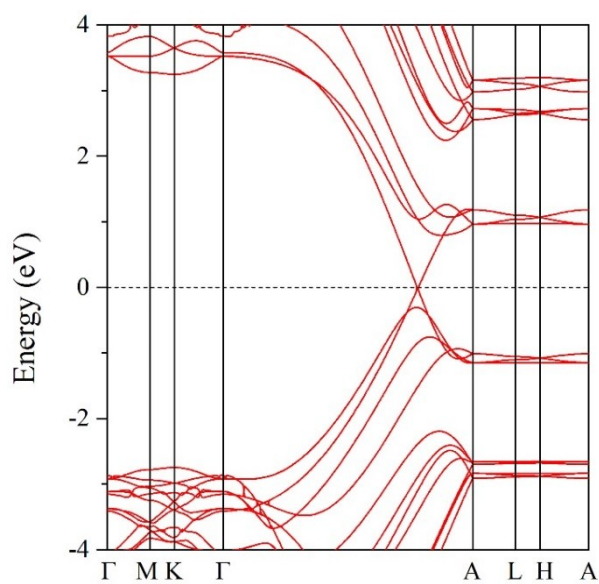


Fig. S6 Electronic band structure of HZGM-42 calculated by using the HSE06 functional.

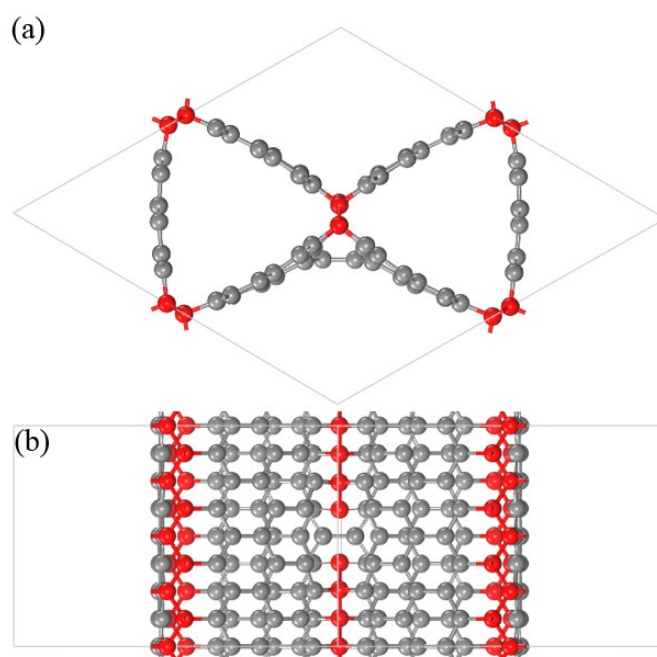


Fig. S7 (a) Top and (b) side views of the optimized structure of HZGM-42 with a mono-vacancy at the sp^3 carbon site. A $1 \times 1 \times 4$ supercell is used.

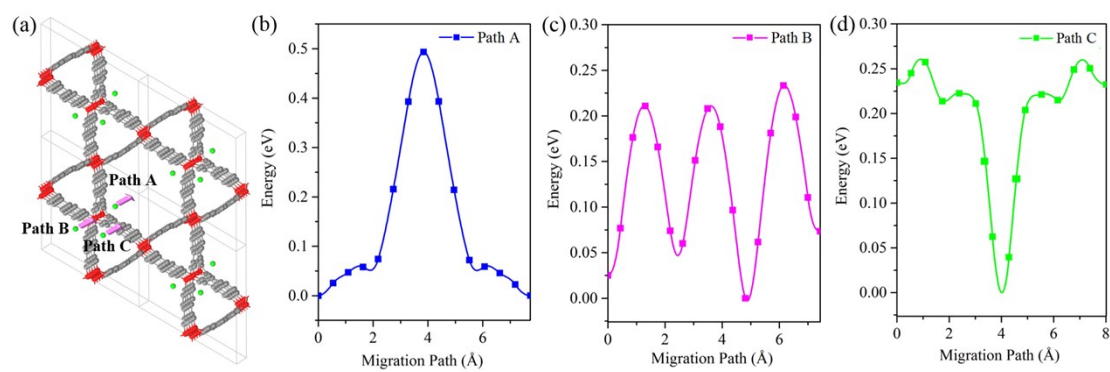


Fig. S8 (a) Three symmetry-inequivalent migration paths of Li diffusion considered along the z-direction around the mono-vacancy at the sp^3 carbon site. (b)-(d) Diffusion energy barrier profiles of the three diffusion paths displayed in (a).

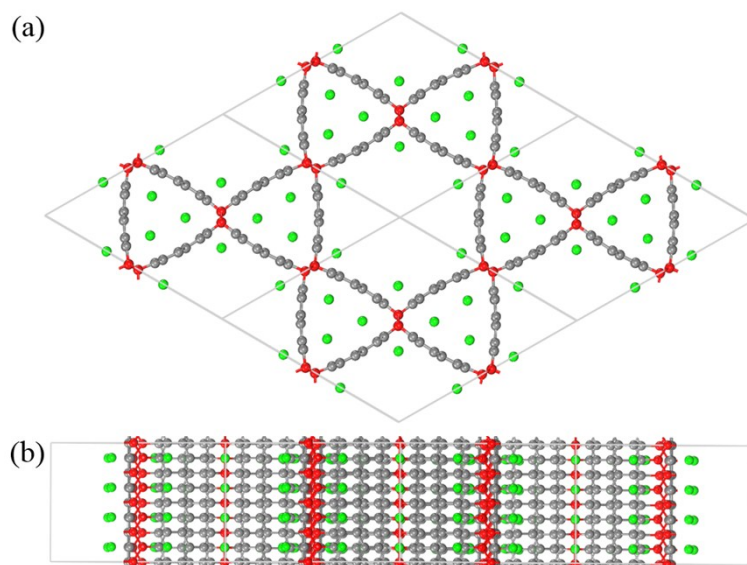


Fig. S9 (a) Top and (b) side views of the full Li-intercalated configuration of HZGM-42. The green, light blue and purple spheres represent lithium ion, sp^2 -, and sp^3 -hybridized carbon atoms, respectively.

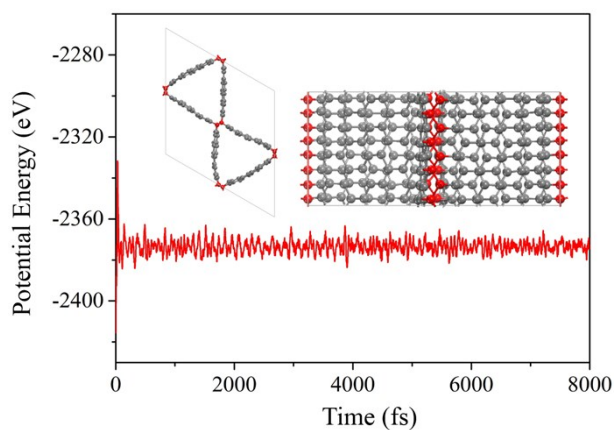


Fig. S10 Total potential energy fluctuation during AIMD simulation at 1200 K of HZGM-66. The inset shows the atomic configurations ($1 \times 1 \times 4$ supercell for HZGM-66) at the end of AIMD simulations at 1200 K.

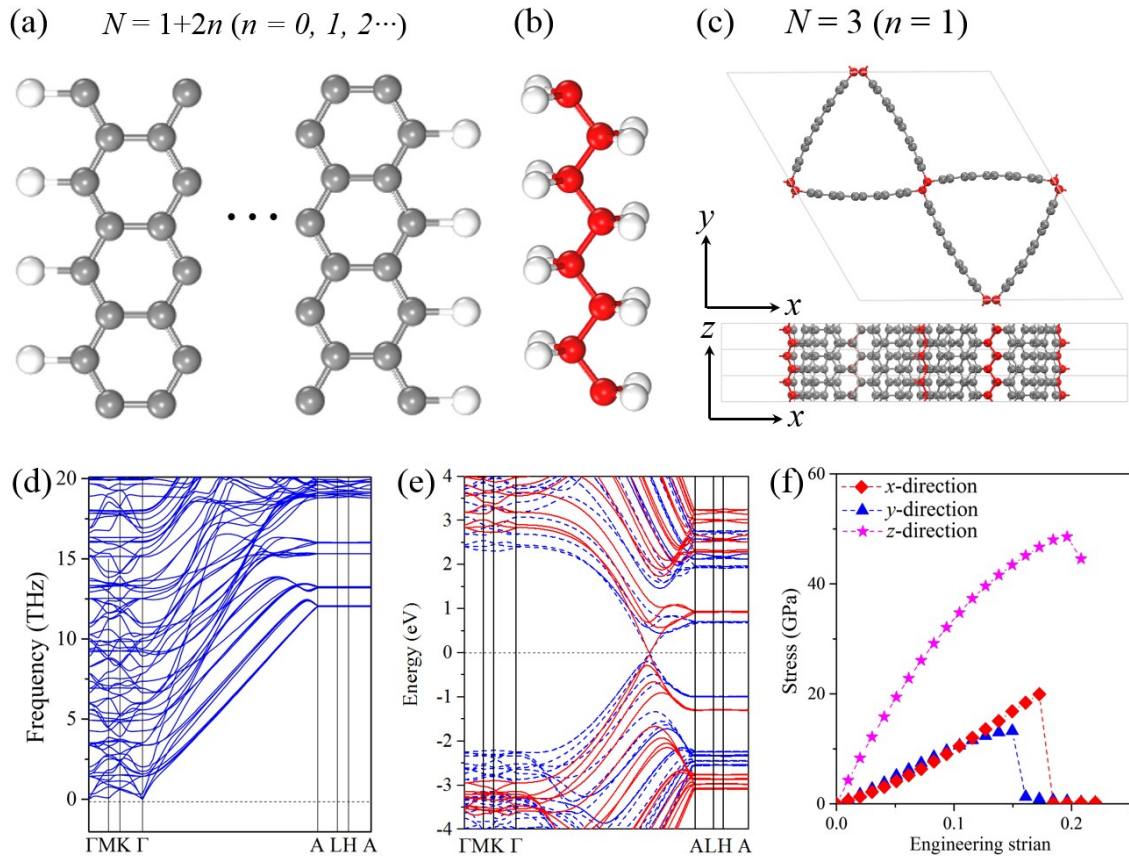


Fig. S11 Two elemental building motifs of HZGM phases, i.e. (a) the graphene nanoribbons with tunable width, and (b) the linkers composed of sp^3 -hybridized carbon atoms. N ($1+2n$) donates the width of the zigzag graphene nanoribbons. (c) Top and side views of HZGM-66 with $N = 3$. (d) Phonon band structure, (e) electronic band structure calculated by DFT-GGA/PBE (blue dashed lines) and the HSE06 hybrid functional (red solid lines), and (f) the orientation-dependent stress-strain relationships of HZGM-66.

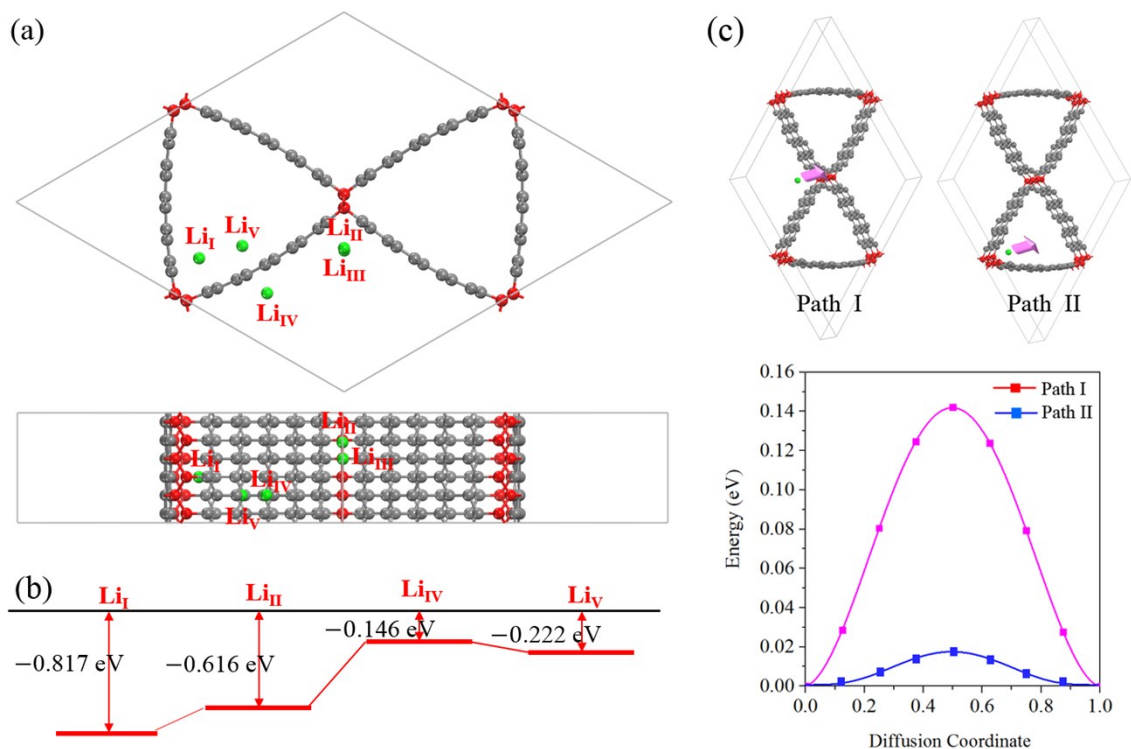


Fig. S12 (a) Top and side views of the possible Li absorption sites for HZGM-66. (b) Binding energies of the four configurations in (a). Configuration Li_{III} changes to Li_{II} after full geometry optimization. (c) Considered migration paths of Li diffusion and the corresponding diffusion energy barrier profiles.

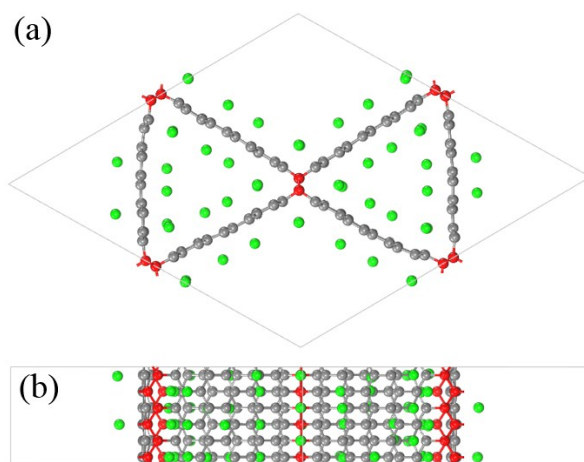


Fig. S13 (a) Top and (b) side views of the full Li-intercalated configuration of HZGM-66.